An Accelerated Augmented Lagrangian Method with application to Compressed Sensing SAR Imaging

H. Emre Güven
ASELSAN, Turkey,
Department of Radar Systems Engineering
heguven@aselsan.com.tr

Müjdat Çetin
Sabancı University, Turkey,
Faculty of Engineering and Natural Sciences,
mcetin@sabanciuniv.edu

Abstract

In this paper we present an accelerated Augmented Lagrangian Method for the solution of constrained convex optimization problems in the Basis Pursuit De-Noising (BPDN) form. The technique relies on on Augmented Lagrangian Methods (ALMs), particularly the Alternating Direction Method of Multipliers (ADMM). Here, we present an application of the Constrained Split Augmented Lagrangian Shrinkage Algorithm (C-SALSA) to SAR imaging, while introducing a method to handle complex SAR imagery in the constrained Total Variation Minimization formulation. In addition, we apply acceleration schemes to C-SALSA to obtain faster convergence of the method; such as used in Fast ADMM methods proposed by Goldstein et al., in the Fast Iterative Shrinkage-Thresholding Algorithm (FISTA) proposed by Beck and Teboulle, and in NESTA proposed by Becker et al. We present examples to illustrate the effectiveness of Accelerated C-SALSA in the context of SAR imaging.

1 Introduction

In this paper we consider the problem of compressed SAR imaging using an Augmented Lagrangian approach to the optimization problem associated with the SAR observation model. There are several sparsity-driven techniques in the context of SAR imaging , though an important factor hindering their use in practice is the excessively high computational cost of solving the associated optimization problem. From this standpoint, it is important to incorporate recent advances in optimization techniques. The motivation for our work comes from our search for such computationally efficient algorithms for compressed sensing in SAR, with a potential for parallel implementation.

As such, Alternating Direction Method of Multipliers (ADMM) techniques have been successfully applied to signal and image recovery problems [1]. ADMM provides a divide-and-conquer approach by splitting unconstrained multi-objective convex optimization problems, augmenting the Lagrangian of the convex optimization problem with a norm-squared error term, and using a non-linear block Gauss-Seidel approach on the resultant terms in the optimization problem. The resulting problem is guaranteed convergence under mild conditions [1].

In this work, we provide a framework for the application of a particular ADMM method, namely the Constrained Split Augmented Lagrangian Shrinkage Algorithm (C-SALSA) [1] to SAR imaging, introduce a method to handle complex SAR imagery in the constrained Total Variation Minimization (TVM) formulation, and apply acceleration schemes to C-SALSA to obtain faster convergence of the method.

2 Background

2.1 SAR Observation Model

The SAR observation model can be considered linear in relating the vector containing the SAR image pixels to the data vector, e.g., consisting of phase history data for spotlight mode SAR imaging. Let us denote the image vector to be constructed by sequentially indexed pixel-values $\mathbf{x} \in \mathbf{C}^N$ and observation kernel by the matrix $\mathbf{B} \in \mathbf{C}^{M \times N}$, which relates $\mathbf{x}$ to the measurement vector $\mathbf{y} \in \mathbf{C}^M$:

$$\mathbf{y} = \mathbf{B}\mathbf{x} + \mathbf{n}, \tag{1}$$

where $\mathbf{n} \in \mathbf{C}^M$ is the additive noise vector, typically from a normal distribution. The data $\mathbf{y}$ can lie in the phase history domain, in which case the matrix $\mathbf{B}$ would be a spatial Fourier transform type operator; or $\mathbf{y}$ can be a conventionally reconstructed image, in which case $\mathbf{B}$ would be a convolution operator representing the point spread function of the entire imaging process. In this paper, the data are assumed to be in the phase history domain, therefore a two-dimensional Fourier transform type model is appropriate for modelling the relation between the data vector and the unknown SAR image vector. In the reconstruction algorithms we use, however, the matrix is never formed explicitly but FFTs are carried out to perform the associated matrix-vector products.

2.2 Sparse reconstruction approaches

In this paper, we consider the application of C-SALSA [1] for the reconstruction of SAR images, as well as an accelerated version thereof. The algorithm is described in the sequel. For the compressed sensing problem, the problem can be cast as

$$\underset{\mathbf{x}}{\text{minimize}} \quad \|\mathbf{B}\mathbf{x} - \mathbf{y}\|_2^2 + \lambda \phi(\mathbf{x}) \tag{2}$$

where $\phi(x)$ is the penalty function appropriately selected according to the reflectivity characteristics of the imaged region. $\phi(\mathbf{x}) = \|\mathbf{x}\|_1$ results in the enhancement of sparsity in the reconstructions; whereas $\phi(\mathbf{x}) = TV(|\mathbf{x}|)$ results in piecewise-smooth reconstructions, TV being the total-variation of the image to be reconstructed [1, 2]. Notice that, the SAR images are complex and the total variation is defined on the magnitude of the SAR image. The handling of complex SAR data requires special care, as will be described in the sequel.

Algorithm 1: *C-SALSA* [1]

1. Set $k = 0$, choose $\mu > 0$, $\mathbf{v}_0^{(1)}, \mathbf{v}_0^{(2)}, \mathbf{d}_0^{(1)}, \mathbf{d}_0^{(2)}$
2. **repeat**
3. $\mathbf{r}_k = \mathbf{v}_0^{(1)} + \mathbf{d}_0^{(1)} + \mathbf{B}^H \left(\mathbf{v}_0^{(2)} + \mathbf{d}_0^{(2)} \right)$
4. $\mathbf{u}_{k+1} = \left(\mathbf{I} + \mathbf{B}^H \mathbf{B} \right)^{-1} \mathbf{r}_k$
5. $\mathbf{v}_{k+1}^{(1)} = \mathbf{\Psi}_{\phi/\mu} \left(\mathbf{u}_{k+1} - \mathbf{d}_k^{(1)} \right)$
6. $\mathbf{v}_{k+1}^{(2)} = \mathbf{\Psi}_{\iota_{E(\epsilon, \mathbf{I}, \mathbf{y})}} \left(\mathbf{B}\mathbf{u}_{k+1} - \mathbf{d}_k^{(2)} \right)$
7. $\mathbf{d}_{k+1}^{(1)} = \mathbf{d}_k^{(1)} - \mathbf{u}_{k+1} + \mathbf{v}_{k+1}^{(1)}$
8. $\mathbf{d}_{k+1}^{(2)} = \mathbf{d}_k^{(2)} - \mathbf{B}\mathbf{u}_{k+1} + \mathbf{v}_{k+1}^{(2)}$
9. $k \leftarrow k + 1$
10. **until** some stopping criterion is satisfied.

An alternative form of the problem is such that the constraint comes from the error in the measurements, where the error norm is prescribed to be smaller than a radius ϵ suggested by the signal-to-noise ratio (SNR) that can be estimated from the data.

$$\begin{aligned} \underset{\mathbf{x}}{\text{minimize}} \quad & \phi(\mathbf{x}) \\ \text{subject to} \quad & \|\mathbf{B}\mathbf{x} - \mathbf{y}\|_2 \leq \epsilon \end{aligned} \tag{3}$$

where $\phi(\mathbf{x})$ is selected as explained above.

3 Accelerated C-SALSA applied to SAR Imaging

In this section, we describe the use of the method C-SALSA in SAR imaging, and an accelerated version thereof. We first start with the description of C-SALSA [1] within the context of SAR imaging.

3.1 C-SALSA

The problem in (3) with $p = 1$ can be expressed in an unconstrained form as [1]:

$$\underset{\mathbf{x}}{\text{minimize}} \quad \phi(\mathbf{x}) + \iota_{E(\epsilon, \mathbf{I}, \mathbf{y})}(\mathbf{B}\mathbf{x}) \tag{4}$$

where $\iota_{E(\epsilon, \mathbf{I}, \mathbf{y})}(\mathbf{B}\mathbf{x})$ is the indicator function of the feasible set $E(\epsilon, \mathbf{I}, \mathbf{y})$ such that

$$E(\epsilon, \mathbf{I}, \mathbf{y}) = \left\{ \mathbf{x} \in \mathbf{C}^N : \|\mathbf{B}\mathbf{x} - \mathbf{y}\|_2 \right\} \leq \epsilon, \tag{5}$$

$$\iota_S(\mathbf{s}) = \begin{cases} 0, & \text{if } \mathbf{s} \in S \\ +\infty, & \text{if } \mathbf{s} \notin S \end{cases}. \tag{6}$$

The steps of C-SALSA are shown in Algorithm 1. The vectors $\mathbf{v}_0^{(1)}$ and $\mathbf{d}_0^{(1)}$ are in $\mathbf{C}^N$, whereas $\mathbf{v}_0^{(2)}$ and

$\mathbf{d}_0^{(2)}$ are in $\mathbf{C}^M$. The operators $\mathbf{\Psi}_{\phi/\mu}$ and $\mathbf{\Psi}_{\iota_{E(\epsilon,\mathbf{I},\mathbf{y})}}$ are the Moreau proximal maps for $\frac{1}{\mu}\phi(\mathbf{x}) = \frac{\|\mathbf{x}\|_1}{\mu}$ and $\iota_{E(\epsilon,\mathbf{I},\mathbf{y})}(s)$ given by

$$\mathbf{\Psi}_{\phi/\mu}(\mathbf{s}) = \text{soft}(\mathbf{y}, 1/\mu), \qquad (7)$$

and

$$\mathbf{\Psi}_{\iota_{E(\epsilon,\mathbf{I},\mathbf{y})}}(\mathbf{s}) = \begin{cases} \mathbf{s}, & \text{if } \|\mathbf{s}-\mathbf{y}\|_2 \le \epsilon \\ \mathbf{y} + \epsilon \frac{(\mathbf{s}-\mathbf{y})}{\|\mathbf{s}-\mathbf{y}\|_2}, & \text{if } \|\mathbf{s}-\mathbf{y}\|_2 > \epsilon \end{cases}, \qquad (8)$$

respectively, where $\text{soft}(\mathbf{y}, 1/\tau)$ denotes the element-wise application of $y_i \to \exp\{\mathrm{j}\angle(y_i)\} \max\{|y_i| - \tau\}$ to entries y_i of $\mathbf{y}$ for $i = 1, \ldots, M$. Here, we have extended the soft-thresholding function to the complex case through multiplication by the phase factor of each entry $\exp\{\mathrm{j}\angle(y_i)\}$ instead of the originally defined factor $\text{sign}(y_i)$ for $y_i \in \mathbf{R}$ [1]. In real image recovery with the TVM formulation, $\mathbf{\Psi}_{\phi/\mu}$ can be performed using Chambolle projections to obtain the corresponding Moreau proximal maps.

3.2 Handling phase in TVM for SAR

While it is possible to use C-SALSA for sparse SAR imaging with a slight modification of the soft thresholding function, the handling of the phase requires further care in the Total Variation Minimization formulation. For image components with piecewise-smooth characteristics, it is well-known that the Total Variation is a more suitable cost function to use within the constrained optimization formulation in (3). For complex imagery, as in the context of SAR imaging, it is important to incorporate the fact that the magnitude of each pixel may be piecewise-smooth, while the phase thereof may be random in each pixel. As such, the cost function $\phi(\mathbf{x})$ in (3) should be selected as:

$$\phi(\mathbf{x}) = TV(|\mathbf{x}|) \qquad (9)$$
$$= \sum_{i,j} \nabla|\mathbf{x}|[i,j], \qquad (10)$$

where

$$\nabla|\mathbf{x}|[i,j] = \sqrt{(D_1|\mathbf{x}|)^2 + (D_2|\mathbf{x}|)^2} \qquad (11)$$

and

$$(D_1|\mathbf{x}|) = |\mathbf{x}[i+1,j]| - |\mathbf{x}[i,j]|, \qquad (12)$$
$$(D_2|\mathbf{x}|) = |\mathbf{x}[i,j+1]| - |\mathbf{x}[i,j]|. \qquad (13)$$

For real imagery, it is possible to use Chambolle's algorithm to obtain the result of the Moreau proximal mapping for the Total Variation function [1]. For complex images, we still use a fixed number (such as five) of steps from Chambolle's algorithm on the magnitude of the image in each iteration, and combine the resulting magnitude with the initial phase at each iteration, i.e.,

$$\left(\mathbf{\Psi}_{TV(|\cdot|)/\mu}\mathbf{s}\right)[i,j] = \exp\{\mathrm{j}\angle(\mathbf{s}[i,j])\} \left(\mathbf{\Psi}_{TV(\cdot)/\mu}|\mathbf{s}|\right)[i,j] \qquad (14)$$

where $\mathbf{\Psi}_{TV(\cdot)/\mu}$ is the Moreau proximal mapping corresponding to the cost function $TV(\cdot)/\mu$, obtained herein using Chambolle projections the same way as in C-SALSA [1]. As a result, we extend the C-SALSA method with Total Variation of real imagery to the case where the objective is the Total Variation of the magnitude of complex imagery.

Regarding the implementation, for SAR imaging problem sizes that are relevant in practice, it is not desirable to form the matrix $\mathbf{B}$ due to prohibitively large dimensions. As such, the most critical in C-SALSA is its fourth step, where a matrix-vector equality is solved in each step of the iterative algorithm. Therefore, it is of utmost interest to perform this computation using fast transforms [1], such as the FFT.

Similar to medical imaging applications such as MRI and CT, SAR imaging can be viewed as an image recovery problem with partial Fourier domain observations, where the samples are available on a polar grid [4]. As a result, following an interpolation in the two-dimensional Fourier transform domain, it is possible to relate the resulting data vector to the SAR image through a 2-D FFT. Hence, the multiplications by $\mathbf{B}$ and $\mathbf{B}^H$ can be performed via 2-D FFT operations (that effectively perform the multiplication by a matrix $\mathbf{U}$ containing the Fourier basis vectors), and a masking operator (that effectively performs multiplication by a matrix $\mathbf{M}$ of size $M \times N$ with $(M < N)$, containing a single nonzero entry that is 1 in each row, so that $\mathbf{MM}^H = \mathbf{I}$) such that $\mathbf{B} = \mathbf{MU}$. Such a matrix satisfies [1]:

$$\left(\mathbf{I} + \mathbf{B}^H\mathbf{B}\right)^{-1} = \mathbf{I} - \frac{1}{2}\mathbf{U}^H\mathbf{M}^H\mathbf{MU} \qquad (15)$$

and therefore step 4 of C-SALSA can be performed at the cost of $O(N\log N)$ multiplications [1]. In the examples in Section 4, (15) is implemented via 2-D FFTs and consequent masking in the Fourier domains as described above.

3

3.3 Accelerated C-SALSA

There are several methods in the convex optimization literature for the acceleration of first-order methods such as FISTA [6] for unconstrained form (2), NESTA [7] for the constrained form (3). Recently, the acceleration methods have been applied in the context of ADMM [8]. In this work, we adapt the acceleration approach in [8] to C-SALSA, which is a specific case of an ADMM. Although C-SALSA has been compared favorably to NESTA in several cases [1], an accelerated version of C-SALSA has not been employed in literature to the best knowledge of the authors of this paper. The algorithm, resulting from the application of the acceleration scheme described in [8], is shown below as Algorithm 2. Herein, we only focus on the acceleration scheme with restart, which is preferred for problems that are not well-conditioned [8], as is the case for many inverse problems.

In the accelerated version of the algorithm, each of the primal and dual variables $\left(\mathbf{v}_k^{(1)}, \mathbf{v}_k^{(2)}, \mathbf{d}_k^{(1)}, \mathbf{d}_k^{(2)}\right)$ need to be stored as well as their accelerated counterparts $\left(\hat{\mathbf{v}}_k^{(1)}, \hat{\mathbf{v}}_k^{(2)}, \hat{\mathbf{d}}_k^{(1)}, \hat{\mathbf{d}}_k^{(2)}\right)$. Therefore the accelerated algorithm has nearly twice as much memory requirement as the original. The computational cost associated with calculating the accelerated variables, however, results in only a marginal increase in the computational cost of each iteration, since the bottleneck of the iterative algorithm remains as the steps where 2-D forward and inverse FFTs are performed.

In the next section, we study the performance of *Accelerated C-SALSA* (AC-SALSA) for SAR imaging problems within the constrained optimization formulation (3) where the objective function is either ℓ_1-norm of the scattering profile, or the Total Variation of its magnitude as in Eq. (9).

4 Results

For the examples, we form the phase history data from reference SAR images obtained from wide-angle, high bandwidth SAR returns [3]. L denotes the bandwidth reduction ratio in each dimension (in terms of the bandwidth used to reconstruct the reference image.) The number of available data samples is $M = L^2 N$, where N is the number of phase history samples in the full-bandwidth data used to form the reference image.

The two reference images used in the experiments were Slicy and ZSU-23-4 from the MSTAR database [5]. Slicy was recovered with the ℓ_1 norm objective

---

Algorithm 2: *Accelerated C-SALSA with Restart*

1. Set $k = 0$, $\alpha_0 = 1$,
   choose $\mu > 0$, $\mathbf{v}_0^{(1)}$, $\mathbf{v}_0^{(2)}$, $\mathbf{d}_0^{(1)}$, $\mathbf{d}_0^{(2)}$
2. **repeat**
3. $\mathbf{r}_k = \mathbf{v}_0^{(1)} + \mathbf{d}_0^{(1)} + \mathbf{B}^H \left(\mathbf{v}_0^{(2)} + \mathbf{d}_0^{(2)} \right)$
4. $\mathbf{u}_{k+1} = \left(\mathbf{I} + \mathbf{B}^H \mathbf{B} \right)^{-1} \mathbf{r}_k$
5. $\mathbf{v}_{k+1}^{(1)} = \mathbf{\Psi}_{\phi/\mu} \left(\mathbf{u}_{k+1} - \mathbf{d}_k^{(1)} \right)$
6. $\mathbf{v}_{k+1}^{(2)} = \mathbf{\Psi}_{\iota_{E(\epsilon, \mathbf{I}, \mathbf{y})}} \left(\mathbf{B}\mathbf{u}_{k+1} - \mathbf{d}_k^{(2)} \right)$
7. $\mathbf{d}_{k+1}^{(1)} = \mathbf{d}_k^{(1)} - \mathbf{u}_{k+1} + \mathbf{v}_{k+1}^{(1)}$
8. $\mathbf{d}_{k+1}^{(2)} = \mathbf{d}_k^{(2)} - \mathbf{B}\mathbf{u}_{k+1} + \mathbf{v}_{k+1}^{(2)}$
9. $c_{k+1} = \|\mathbf{u}_{k+1} - \mathbf{v}_{k+1}^{(1)}\|_2^2 + \|\mathbf{B}\mathbf{u}_{k+1} - \mathbf{v}_{k+1}^{(2)}\|_2^2$
10. $\alpha_{k+1} = \frac{1 + \sqrt{1 + 4\alpha_k^2}}{2}$
11. $\hat{\mathbf{v}}_{k+1}^{(i)} = \mathbf{v}_{k+1}^{(i)} + \frac{\alpha_k - 1}{\alpha_{k+1}} (\mathbf{v}_{k+1}^{(i)} - \mathbf{v}_k^{(i)})$, $i = 1, 2$
12. $\hat{\mathbf{d}}_{k+1}^{(i)} = \mathbf{d}_{k+1}^{(i)} + \frac{\alpha_k - 1}{\alpha_{k+1}} (\mathbf{d}_{k+1}^{(i)} - \mathbf{d}_k^{(i)})$, $i = 1, 2$
13. $k \leftarrow k + 1$
14. **until** some stopping criterion is satisfied.

$\phi(\mathbf{x}) = \|\mathbf{x}\|_1$, whereas the SAR image of ZSU-23-4 was recovered with $\phi(\mathbf{x}) = TV(|\mathbf{x}|)$ in the constrained optimization formulation (3).

The signal to noise ratio in all measurements were set to 20 dB, and the iterations were repeated 250 times in all cases. Figure 1 shows the Slicy reconstruction performance for the case with $L = 3/8$, whereas Figure 2 shows the change in the objective vs iteration count. Both for C-SALSA and AC-SALSA, the optimum value is obtained in nearly 100 iterations, and the sparsity of the image is visibly improved with respect to the conventional reconstruction. The objective goes down slightly more quickly for AC-SALSA, especially in the early steps of the algorithm.

Figures 3-5 show the reconstructed SAR images of ZSU-23-4 for the different cases with $L = 3/8$, $L = 2/8$, and $L = 1/8$, respectively. Due to the use of the Total Variation of the magnitude as the objective $\phi(\mathbf{x}) = TV(|\mathbf{x}|)$, there is a slight improvement in contrast both for C-SALSA and AC-SALSA, with respect to the conventional reconstruction, in all three cases. (The objective is about 1.5 times smaller for the solution of optimization problems, in comparison to conventional reconstruction.) Figures 6-8 show the change in the objective for each case with respect to iteration count. The objective goes down more rapidly in AC-SALSA, as compared to C-SALSA.
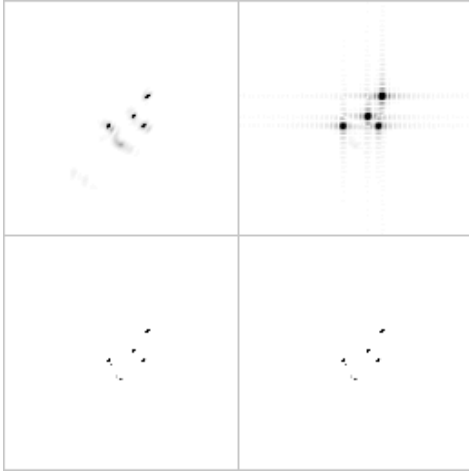
Figure 1: Slicy SAR image reconstruction ($L = 3/8$): reference image (upper-left), conventional reconstruction (upper-right), C-SALSA (lower-left), AC-SALSA (lower-right)
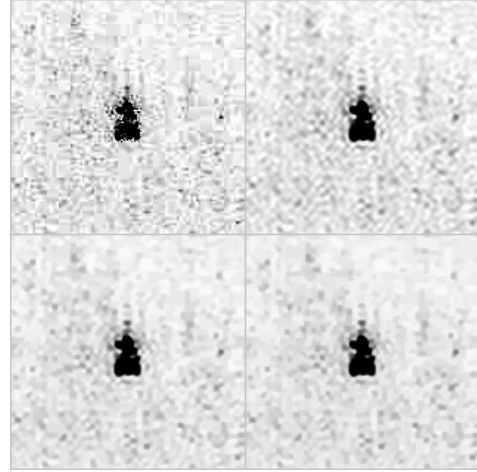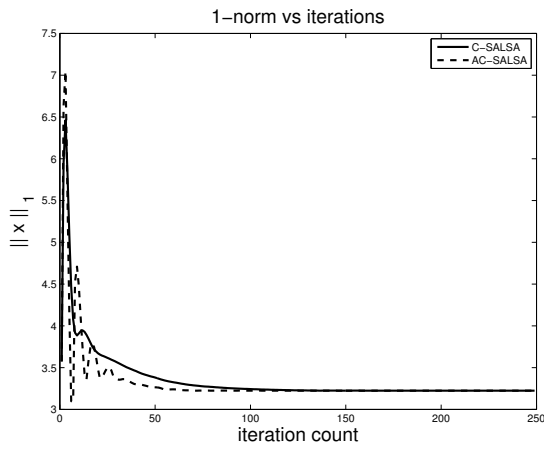

Figure 3: ZSU-23-4 SAR image reconstruction ($L = 3/8$): reference image (upper-left), conventional reconstruction (upper-right), C-SALSA (lower-left), AC-SALSA (lower-right)

Figure 2: Objective $\phi(\mathbf{x}) = \|\mathbf{x}\|_1$ versus iterations for Slicy SAR image reconstruction ($L = 3/8$)
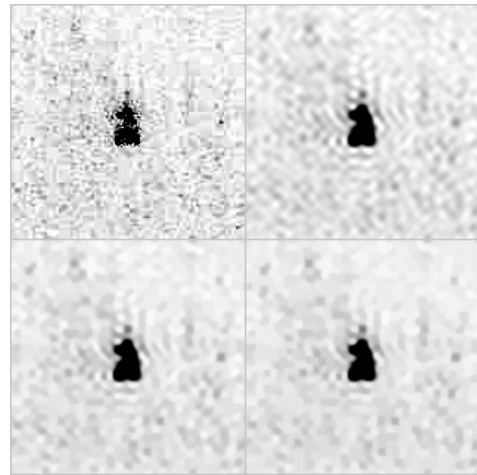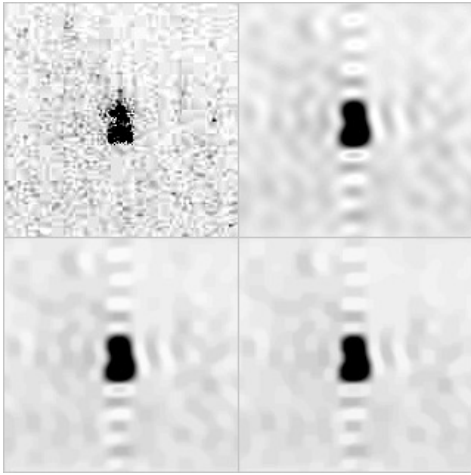

Figure 4: ZSU-23-4 SAR image reconstruction ($L = 2/8$): reference image (upper-left), conventional reconstruction (upper-right), C-SALSA (lower-left), AC-SALSA (lower-right)

5

Figure 5: ZSU-23-4 SAR image reconstruction ($L = 1/8$): reference image (upper-left), conventional reconstruction (upper-right), C-SALSA (lower-left), AC-SALSA (lower-right)
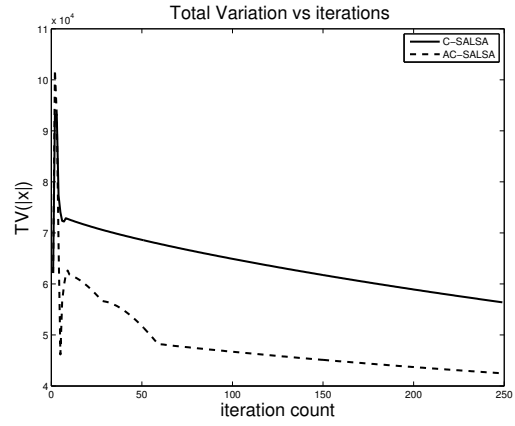

Figure 7: Objective $\phi(\mathbf{x}) = TV(|\mathbf{x}|)$ versus iterations for ZSU-23-4 SAR image reconstruction ($L = 2/8$)
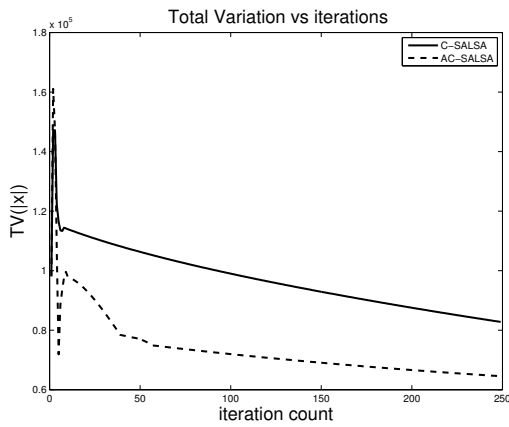

Figure 6: Objective $\phi(\mathbf{x}) = TV(|\mathbf{x}|)$ versus iterations for ZSU-23-4 SAR image reconstruction ($L = 3/8$)
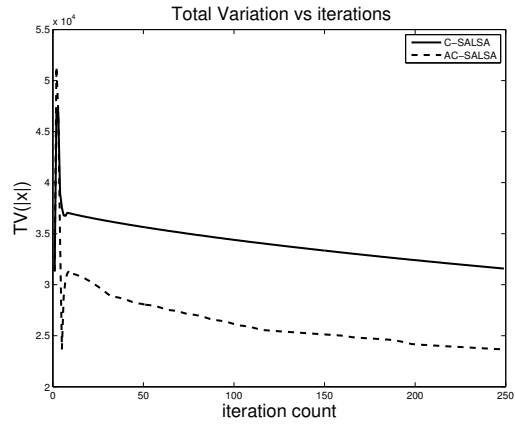

Figure 8: Objective $\phi(\mathbf{x}) = TV(|\mathbf{x}|)$ versus iterations for ZSU-23-4 SAR image reconstruction ($L = 1/8$)

5 Discussion

The faster convergence of the proposed AC-SALSA in comparison to C-SALSA is promising, especially for cases with larger image sizes, where speed of computation limits the number of iterations that can be performed within an operational time-budget. In conclusion, AC-SALSA provides a favorable alternative to C-SALSA in cases where a trade-off between memory and computation time is made possible by the available hardware.

References

[1] M. Afonso, J. M. Bioucas-Dias, M. A. T. Figueiredo, "An Augmented Lagrangian approach to the constrained optimization formulation of imaging inverse problems," *IEEE Trans. Image Processing*, vol. 20, no. 3, pp. 681–695, March 2011.

[2] M. Cetin, W. C. Karl, "Feature-enhanced synthetic aperture radar image formation based on nonquadratic regularization," *IEEE Trans. Image Processing*, vol. 10, no. 4, pp. 623–631, April 2001.

[3] R. L. Moses, L. Potter, and M. Çetin, "Wide Angle SAR Imaging," *SPIE Defense and Security Symposium, Algorithms for Synthetic Aperture Radar Imagery XI*, Eds., E. G. Zelnio and F. D. Garber, Orlando, Florida, April 2004.

[4] C. V. Jakowatz, Jr., D. E. Wahl, P. H. Eichel, D. C. Ghiglia, and P. A. Thompson, *Spotlight-Mode Synthetic Aperture Radar: A Signal Processing Approach*, Norwood, MA: Kluwer, 1996.

[5] Air Force Research Laboratory, Model Based Vision Laboratory, Sensor Data Management System MSTAR Web Page: `www.mbvlab.wpafb.af.mil/public/sdms/data sets/ mstar`.

[6] A. Beck and M. Teboulle, "A fast iterative shrinkage-thresholding algorithm for linear inverse problems," *SIAM Journal on Imaging Sciences*, vol. 2, no. 1, pp. 183–202, March 2009.

[7] S. Becker, J. Bobin, and E. CandŔs, "NESTA: A fast and accurate first-order method for sparse recovery," *SIAM J. Imag. Anal.*, vol. 4, pp. 1–39, 2011.

[8] T. Goldstein, B. Donoghue, S. Setzer, and B. Baraniuk, "Fast alternating direction optimization methods," *CAM Report*, pp. 12–35, UCLA, 2012.